Supplementary Materials: Electric field switching of chiral phonons

MICHAEL GRIMES*[1], HIROKI UEDA[1], CLIFFORD J. ALLINGTON[1], CARL P. ROMAO[2], KURT KUMMER[3], PUNEET KAUR[4], LI-SHU WANG[4], YAO-WEN CHANG[4], JAN-CHI YANG[4,5], SHIH-WEN HUANG[1], AND URS STAUB*[1]

1. Paul Scherrer Institut, 5232 Villigen, Switzerland

2. Czech Technical University in Prague, Prague 120 00, Czech Republic

3. ESRF - The European Synchrotron, 71 Avenue des Martyrs, F-38000 Grenoble, France

4. Department of Physics, National Cheng Kung University, Tainan 701, Taiwan

5. Center for Quantum Frontiers of Research & Technology (QFort), National Cheng Kung University, Tainan 701401, Taiwan

*E-mails: michael.grimes@psi.ch, urs.staub@psi.ch

S1 - Sample Characterisation

The free-standing films of Barium Titanate (BTO) were placed on bottom electrodes composed of gold and copper before the top electrodes were prepared on top using lithography, see Figure 2 in the main text. The electrode stack structure is presented in the left panel of Figure 1. The orientation of the BTO membrane was confirmed prior to the resonant inelastic x-ray spectroscopy (RIXS) experiments using a standard lab diffractometer (D8 DISCOVER Bruker). As can be seen in the right panel of Fig. 1, the expected out-of-plane orientation was confirmed to be (001) as seen from the visible peaks (001) and (002), where the *P4mm* (tetragonal) structure [1] allows for both peaks to be observed. From estimates of the structure factor, the relative Bragg peak intensities are commensurate with the predicted structure. The peak intensity of a Bragg peak, *hkl*, is found from the square of the structure factor over the N atoms in the unit cell,

$$F_{hk\ell} = \sum_{j=1}^{N} f_j \mathrm{e}^{[-2\pi i(hx_j + ky_j + \ell z_j)]}, \tag{S1}$$

where x_j, y_j, z_j and f_j represent the co-ordinates and x-ray scattering factor, respectively, of atom i. The ratio I_{001}/I_{002} found experimentally (0.31) was slightly less than predicted from bulk (0.55). We attribute this to strain relief in the ferroelastic free-standing films [2] as compared to values in the literature which are measured from either epitaxial thin films [3] or bulk[1].

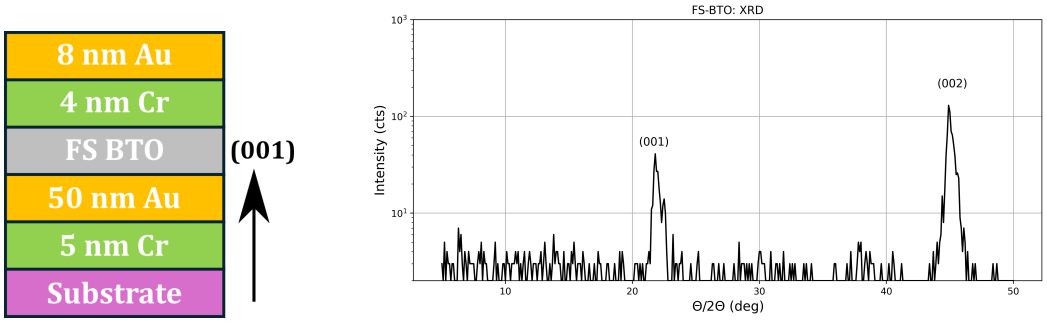

Supplementary Figure 1: Left: Sketch of the sample stucture where the (001) direction of BTO is out of plane. Right: Determination of the out-of-plane orientation was confirmed with a $\theta/2\theta$ scan of the free-standing BTO film performed with lab-based diffractometer

The intensity of non-specular peaks could not be compared to the above due to difficulties in aligning the sample with the lab-based system, possibly due to the sample thickness (80 nm). However, a qualitative overview of in-plane order is shown in Figure 2 where the [103] peaks are plotted as the sample azimuthal angle, ϕ, is swept across $\pm$ 120 degrees.

These show the expected 90 degree offset for the tetragonal crystal structure where the (010) is along the film edge (see Figure 2 in the main text).

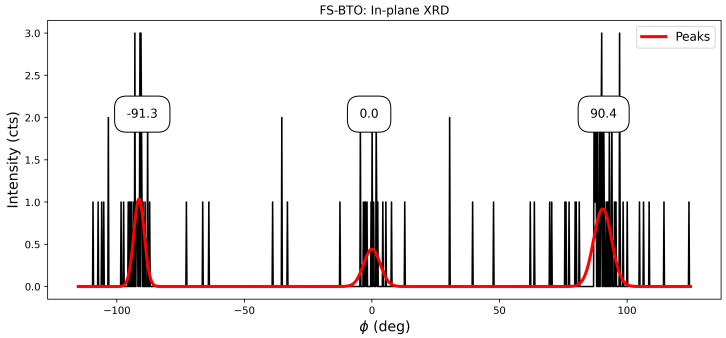

Supplementary Figure 2: In-plane scan of the sample azimuthal angle for the [103] peak of FS-BTO film.

S2 - X-ray absorption spectroscopy

Prior to the RIXS measurements we first investigated the edge and near edge regions of the oxygen K-edge using x-ray absorption spectroscopy (XAS). This edge occurs at the energy expected and was used as a reference for the choice of the x-ray energies for RIXS. During the RIXS measurements, XAS scans were intermittently recorded to adjust for energy drift in the x-rays produced by the synchrotron. In all instances, the XAS spectra are recorded on a portion of film that is un-poled (≈ 0.1 mm from the electrodes) The cumulative spectra over the course of the experiment is shown in Figure **3** where the error bars represent standard deviation of the signal. The energy drift is corrected according to the mid-point of the leading edge.

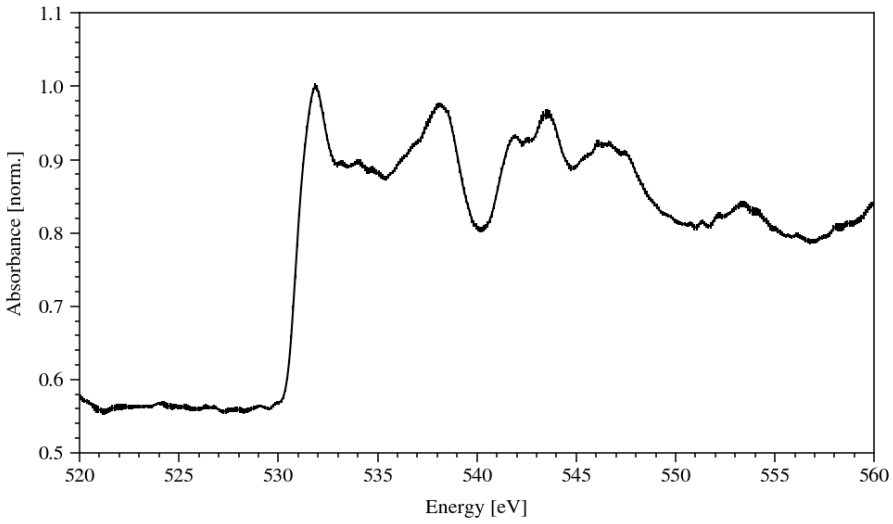

Supplementary Figure 3: XAS of the BTO film. Data was acquired intermittently over a period of 16 hours during one set of RIXS measurements. The error bars are found from the standard deviation of the binned data when corrected according to the leading edge.

S3 - Resonant inelastic x-ray scattering

S3.1 - Theory of CD RIXS

We present here a brief over view of the origin of circular dichroism that emerges in RIXS from the basis of circular rotation of ions in the unit cell. The interested reader is referred to the paper of Ueda *et al.* for a detailed derivation [4].

The RIXS process involves the absorption of an incident photon and emission of scattered photon which have momenta, $\mathbf{Q}$, and $\mathbf{Q}'$, and polarisations, ϵ, and ϵ'. During the process, the intermediate core-hole state can impart a net momentum, $\mathbf{q}$ and energy, E_m, to the system. Therefore, a theoretical model for a RIXS process requires in general: the Hamiltonians; $\mathcal{H}_0$, $\mathcal{H}_1$ of the initial and finals states, and the interaction Hamiltonian of the intermediate state, $\mathcal{H}_i$, and the dipole operators, D_ϵ and $D_{\epsilon'}$, creating/annihilating the intermediate state exciton, respectively, that are functions of the incident and scattered x-ray polarisations. Since we consider the oxygen K-edge which involves the 1s to 2p transition, the rotational motion of the ions is described in terms of the p orbitals where the non-centrosymmetric nature of the unit cell imposes that the p_y and p_z orbitals are non-degenerate. One may construct the system as a quantum pendulum as a function of the angle, ϕ. The creation operators in this case are written as $p^+_{\phi+} = p^+_y \cos(\phi) + p^+_z \sin(\phi)$. This results in an intermediate state,

$$\mathcal{H}_i = -\beta \; ss^+p^+(\sigma_z \cos 2\phi + \sigma_y \sin 2\phi)p, \tag{S2}$$

where σ denotes the Pauli matrices. By following the Kramers-Heisenberg formula and assuming ultrashort core-hole lifetime (UCL) with respect to the circular motion of the ions, one can arrive at the following estimation of the RIXS amplitude due to the chiral phonon modes, m, as

$$A^{\mathrm{UCL}}_m \propto \langle m|(\epsilon'_c)^* \begin{pmatrix} 0 & e^{-2i\phi} \\ e^{2i\phi} & 0 \end{pmatrix} \epsilon_c|0\rangle \,, \tag{S3}$$

where we introduce a circular polarisation basis as $\epsilon_c = (\epsilon_z + i\epsilon_y, \epsilon_z - i\epsilon_y)$. One can derive that the difference in amplitude for right and left handed photons is maximised as $2\hbar$. We re-iterate that the conditions imposed by the circular basis imply that the contrast can only be observed when inversion symmetry is broken in the unit cell with respect to the motion of the oxygen ions. Likewise, the inversion of the Ti ion displacement will reverse the contrast as the projection of the oxygen p_y and p_z orbitals will be inverted.

S3.2 - Energy dependence

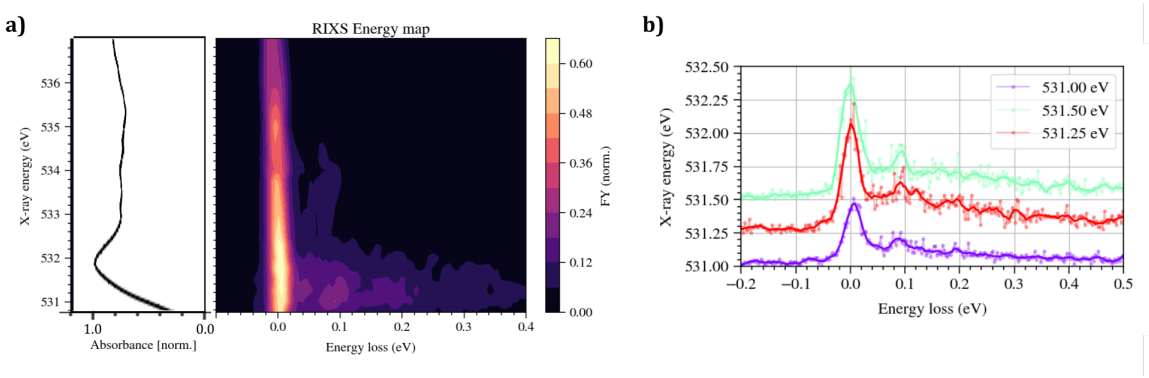

Supplementary Figure 4: a) Right: Energy map of the RIXS signal near the elastic line for q_4 = (0.04, 0.23, 0.42) Å^{-1}. The left-/right-handed portions show the spectra near the leading edge and within the inter-peak region, respectively. Left: Energies of the spectra are plotted with respect to the XAS (performed on a portion of the BTO film that is un-poled). b) Selected RIXS spectra in near edge region

The energy dependence of the phonon fingerprints in the RIXS spectra was investigated to optimise the detection of the chiral phonon dichroism signal. The spectra in Figure 4 show the changes observed in the signal as the x-ray energy is swept from the near edge (530 eV) of the oxygen K-edge up to the higher energy features (540 eV) in the XAS spectra. The left portion of Fig. 4 a) illustrates where on the XAS spectra these energies correspond. It is seen that the elastic line in the spectra is strongest near the XAS peak while the inter-peak regions have lower overall signal (left- and right-hand portions of Fig. 4, respectively). The phonon fingerprint is discussed in detail in the main paper and in latter sections (see S4), comprising the low energy features up to 0.2 eV in the RIXS spectra. These features are strongest for x-ray energies in the near edge region. That these relaxation signals are found below the peak resonance has been previously seen in RIXS studies [4, 5].

A select range of spectra are shown in Fig. 4 b) where the phonon features are especially pronounced. The acquisition time was increased by a factor of ten to improve the SNR. These are found in the near-edge region. For the main paper, the x-ray energy was set at 531.25 eV for all RIXS measurements to ensure the strongest chiral phonon contribution to the CD experiments. The energy map can be seen in the right portion Fig. 4 a).

S3.3 - Circular dichroism in RIXS

In order to attribute the observed circular dichroism to the presence of chiral phonons, we first must discount other source of contrast. While dichroisms can indicate that a transfer of angular momentum has occurred which is the case in XMCD for example, the RIXS process is also sensitive to sample anisotropies which can present in the refractive index for example. For instance, the tetragonal structure of the BTO sample imposes a difference in the scattering for in-plane and out of plane interactions. Following the work of Nag *et al.*, the sample birefringence can induce CD which will depend on the incident angle, θ_i, of the x-rays with respect to the optical principal axis [6]. Through the sample depth, the Stokes parameters (see main text) of the C+ and C- light will vary as the light travels a distance $l_i = t/\sin\theta_i$. The polarisation state of the light is computed as:

$$P_{li} = {}^{I_{li}}/_{I_0} T_i P T_i^{\dagger}. \qquad \text{(S4)}$$

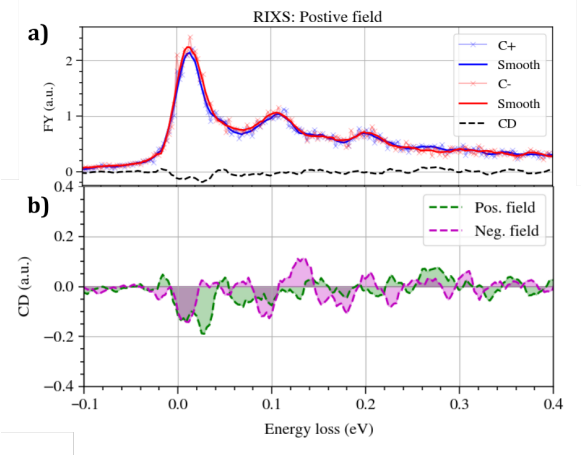

Supplementary Figure 5: a) Example of the RIXS spectra for two different circular polarisations of x-rays for $\vec{q}$ = [0.247, -0.402, 0.557] r.l.u.. Aside from the incident angle, all other parameters are held constant as compared to the measurements in Fig. 3 of the main text. b) The circular dichroism of the BTO sample when positive and negative fields are applied. The field switching is less apparent, though some contrast is observed near the low energy phonons.

Therefore if one performs experiments where the x-rays are not of normal incidence, a more sophisticated analysis is required to extract the relevant CD contrast. For example, we show the measured RIXS contrast when an incident angle of 20 ° is used in Figure **5**, equivalent to $\vec{q}$ = [0.247, -0.402, 0.557] r.l.u. A strong contrast can be seen across the whole spectrum, and also across the elastic line. In contrast to Fig. 3 of the main text, when we measure the effect of field switching, the contrast is not reversed. Instead it is dominated by the effects of birefringence, see Fig. **5**b). Finally, we note that the CD signal at the phonon peaks is much stronger here than is shown for the measurements performed in the main text. However, it is preferable to be solely sensitive to the contrast from chiral phonons.

S3.4 - Measurement Procedure

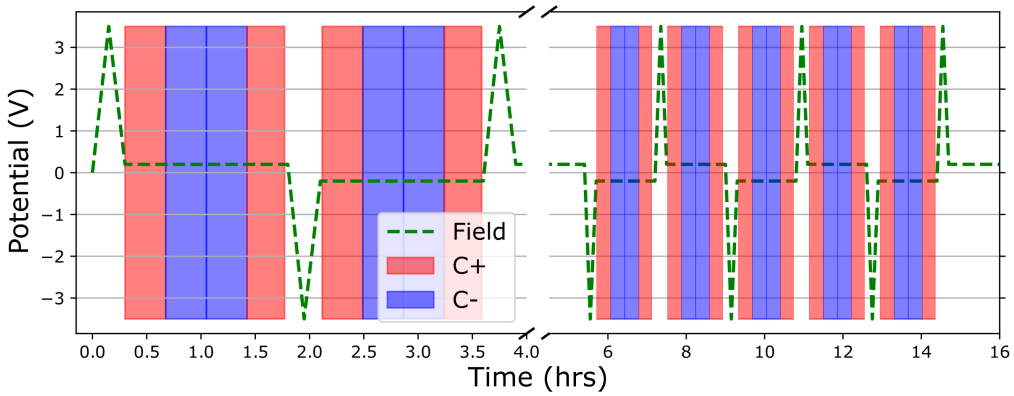

Supplementary Figure 6: Measurement scheme used during the experiment. The polarisation is switched by applying +(-) 3.5 V before a +(-) 0.2 V holding potential is maintained. In each ferroelectric state, RIXS is measured with circularly right- and left-handed x-rays in a '+ - - +' pattern.

In order to mitigate drift in the CD signal during data acquisition over a period of many hours, we implement a measurement procedure which swithces between C+ and C- light in a '+ - - + pattern, as seen in Figure 6. The ferrolecrtic domains are switched using the write voltage while a small holding potential ensures that small fluctuations don't disturb the polarisation within the area of the contact pad (see Fig. 2 in the main text).

S3.4 - Data treatment and error calculations

In the measurement of RIXS data, a 2D detector is used where the number of photons impinging on each pixel is collected. The spacing of the pixels is finer than the energy resolution of the x-ray source, meaning that we are in fact measuring it with too much precision. In such cases, one must either smooth or re-bin the data to emulate more correctly the experimental parameters. As the experimental resolution is not an integer multiple of the probed resolution, we use a simple Savitzky-Golay function to smooth the data across the detector pixels. This smoothed line is what is presented in the main text as the RIXS spectra (see Figure 3). For the calculation of the uncertainty of the signal, the smoothed data is not ideal as the standard Gaussian error propagation would require a function which weights the contribution of every point to each data point.

Instead, for the uncertainty, we start by re-binning the data (by a factor of 2) and then estimating the standard deviation of the binned data across the number of scans performed. This is done independently for each combination of C+/C- x-rays and positive/negative electric fields. The uncertainty in the contrast shown in the lower portion of Fig. 3 in the main text is simply the Gaussian propagated error:

$$\sigma_{CD} = \sqrt{\sigma_{C+}^2 + \sigma_{C-}^2 - 2\sigma_{C+C-}}, \tag{S5}$$

where $2\sigma_{C+C-}$ is zero (as they are measured independently in a '+ - - +' sequence). The error for the XAS data is computed in a similar manner.

S4 - DFT calculations

Density functional theory (DFT) calculations were performed using Abinit v. 10. The tetragonal structure is implemented by relaxing the structure in the P4mm space group, corresponding to the symmetry of the material under ambient conditions. The resulting phonon distribution is shown in Figure 7, where the lowest lying phonon modes are seen to have negative energy indicating the thermally excited state. The colour scale used refers to the degree of chirality of the phonon modes. This is computed over the n atoms in the unit cell as:

$$\mathbf{S}_z = \sum_{m=1}^{n} \mathbf{S}_{z,m} = \sum_{m=1}^{n} \left(|\langle \mathbf{r}_{m,z} | \epsilon_m \rangle|^2 - |\langle \mathbf{l}_{m,z} | \epsilon_m \rangle|^2 \right), \tag{S6}$$

where $\mathbf{S}_z$ is the z component of the mode, ϵ_m are the phonon eigenvectors, and $\mathbf{r}_{m,z}$, $\mathbf{l}_{m,z}$ are the right- and left-handed circular rotation projections of each atom, m, respectively. The total phonon angular momentum is then computed as $\mathbf{J} = \hbar\mathbf{S}$, based on the formalism of Zhang *et al.* [7].

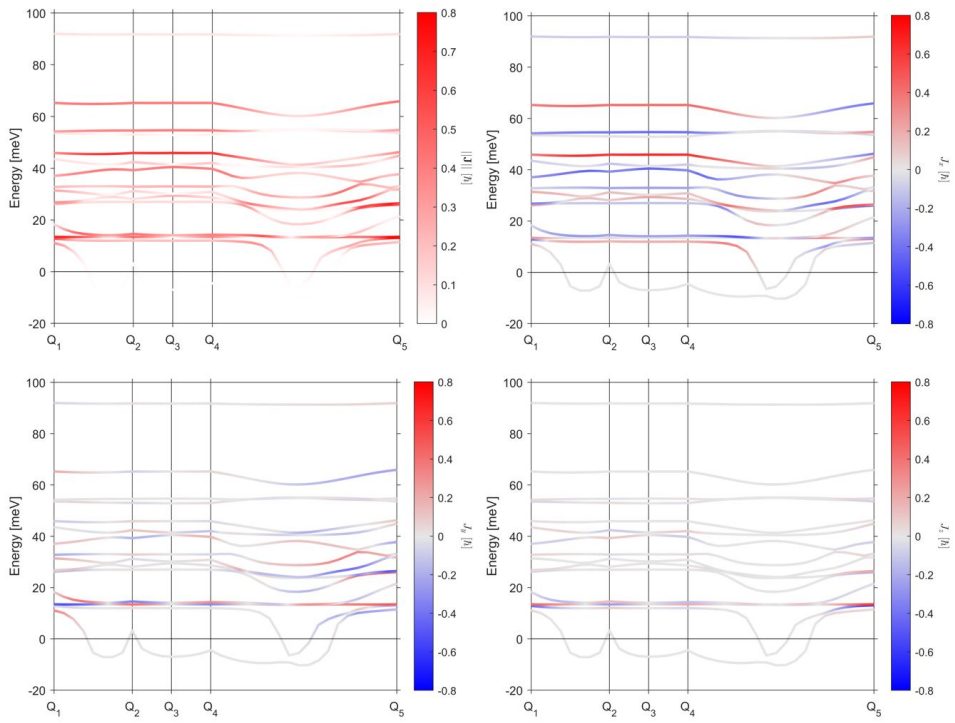

Supplementary Figure 7: Phonon band structure of BTO coloured according to the magnitude, ||**S**||. (a) and x, y, and z components (b–d) of the phonon circular polarization vector, **S**, for the measured Q-points.

We further present the phonon magnetic moments in Figure 8. The phonon magnetic moment is estimated as that generated by a circular charge current of the ions being written as [8]

$$\mathbf{m}^{ph}_{\nu\mathbf{q}} = \sum \mathbf{m}^{ph}_{\nu\mathbf{q}\alpha} = \hbar \sum \frac{eZ^*_\alpha}{2\mathcal{M}_\alpha} \mathbf{l}^{ph}_{\nu\mathbf{q}\alpha}, \tag{S7}$$

where Z^*_α are the Born effective charge tensors, $\mathcal{M}_\alpha$ are the masses of the atoms α in the unit cell [9]. Finally, the plotted values refer to the moments $\mu_{ph} = |m_i|$ for $i = x, y, z$.

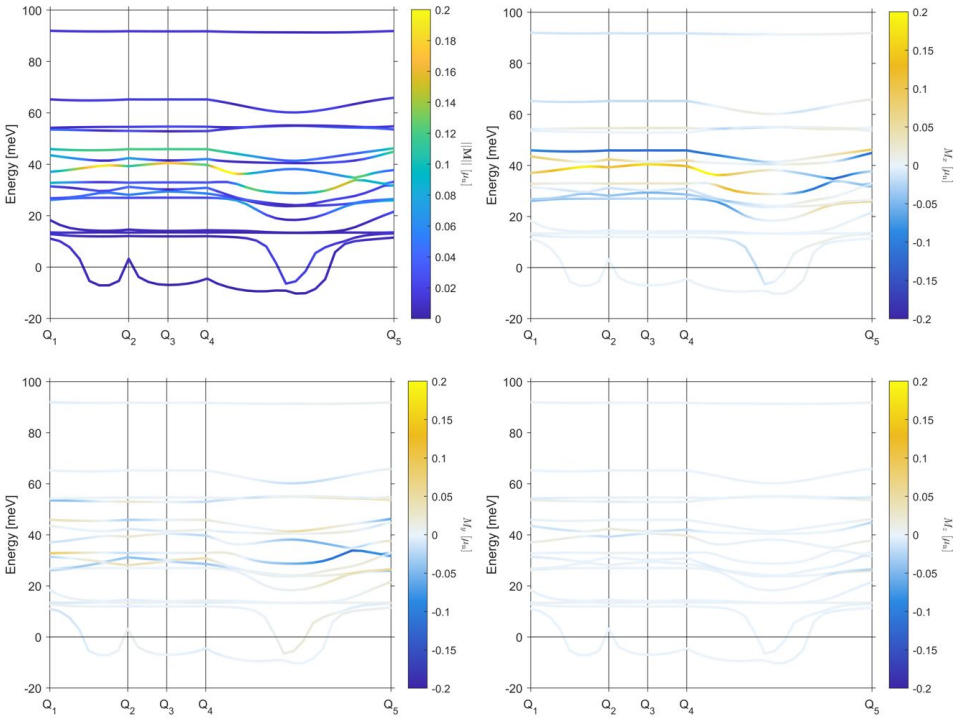

Supplementary Figure 8: Phonon band structure of BTO coloured according to the magnitude ($||\mu||$). (a) and x, y, and z components (b–d) of the phonon magnetic moment (μ), given in units of the nuclear magneton, for the measured Q-points.

In order to estimate the expected RIXS signal from a selected phonon mode, I_{ph}, one can consider the modulation of the local electronic potential. For infrared-active modes, the intermediate excited state will be sensitive to the electron-phonon coupling, $g_{q,\epsilon}$, (under the Franck-Condon principle [10]) as

$$I_{ph}(\mathbf{q},\omega) \propto |g_{q,\epsilon}|^2 \approx |Z^*_\epsilon|^2 \,. \tag{S8}$$

The Born effective charge tensors, Z^*, are calculated using Eq. 53 of Gonze *et al.* [11]. This can simply be described as the linear relation between the force on the ions, and the macroscopic electric field, $\mathcal{E}$, i.e.

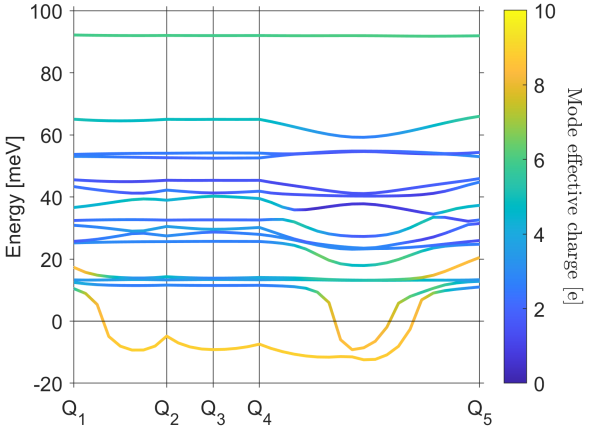

Supplementary Figure 9: Mode effective charges of the phonon modes as predicted from DFT.

$$Z^*_{m,\beta\alpha} = \frac{\partial F_{m,\alpha}}{\partial \mathcal{E}_\beta}, \tag{S9}$$

where β represents the direction of the polarisation, and α the direction of the atoms in the sublattice. For each mode, the ionic displacement is used to generate the mode effective charge where we plot the modulus of this complex vector in Figure 9. An equivalent treatment of Raman-active phonon would begin from an estimation of the mode polarisability, $\left|\frac{\partial Z^*_\epsilon}{\partial \mathcal{E}}\right|^2$. In each instance, the magnitude of $\mathbf{q}$ described in the main text are indicated as $\mathbf{q}_1$, $\mathbf{q}_2$, $\mathbf{q}_3$, and $\mathbf{q}_4$.

We focus on three phonon modes of BTO which are expected to have significant angular momentum. For each mode, the chiral motion as well as the projection parameter, $\mathbf{J} \cdot \mathbf{q}$, is calculated as a function of $\mathbf{q}$ while the azimuthal angle is rotated. However, one must first consider the experimental energy resolution that is present in the RIXS measurements. As discussed in the main paper, we are not able to resolve single phonon modes in the measurements and the contrast will be a convolution of the phonon modes within a given energy range (instrumental resolution). The resulting outputs of the convolved modes are shown in Figure 10. In each case, the central $\mathbf{q}$ vectors used in the experiment are indicated on the figures. We note the C_{4V} symmetry. In Figure 11, the strongest contrast is expected for the two lower lying modes, while the higher energy phonon mode (100 meV) possesses a lower degree of chirality. This reflects the contrast seen in the RIXS experiments.

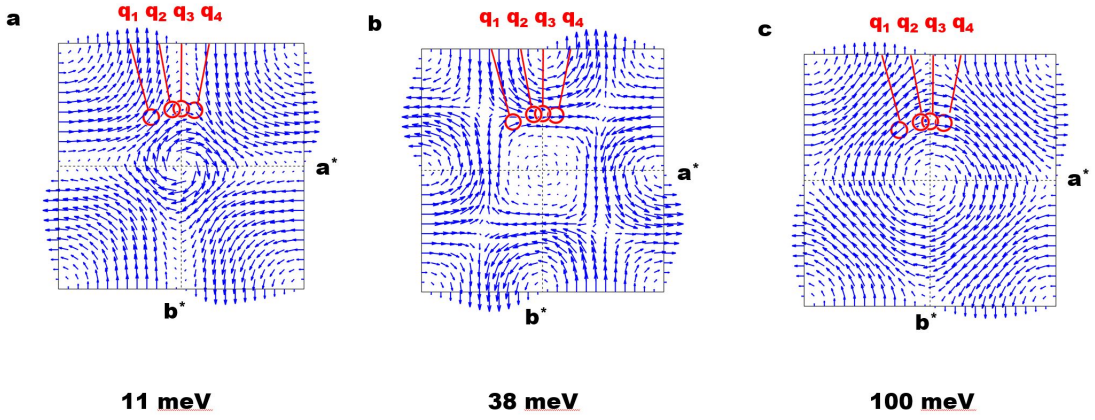

Supplementary Figure 10: Phonon angular momentum vectors.

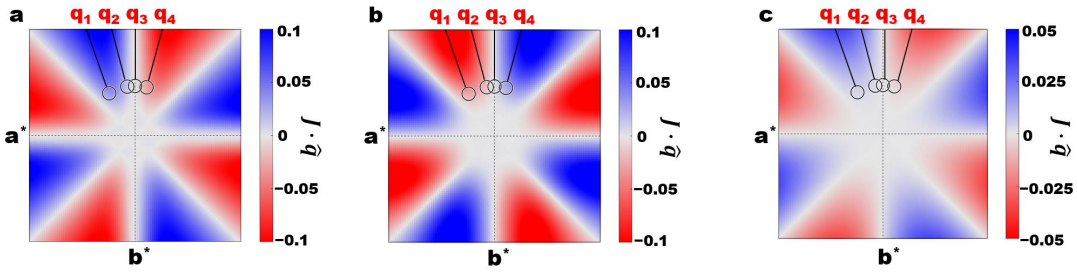

Supplementary Figure 11: Chiral projection of the modes, defined as $\mathbf{J} \cdot \mathbf{q}$. The C_{4V} symmetry of the lattice is observed for the three phonon modes, where the angular momentum is zero at high-symmetry points.

In Figure 12, we attempt to combine several phonon modes around the chiral modes and compute the average chiral motion for the slice of q-space upon which our **q** points lie. These are weighted by the magnitude of the mode effective charges which will reflect the sensitivity of RIXS to each eigenmode. In general this compares well to that shown in Fig. 4 of the main paper. The one exception is the reduced contrast at position $\mathbf{q_1}$ for the lowest energy phonon. At this point, the contrast may not be resolved well. However, this meant we could use the chiral projections, $\mathbf{J} \cdot \mathbf{q}$, to compare with our measured results in Fig. 4 of the main paper, to a good first approximation.

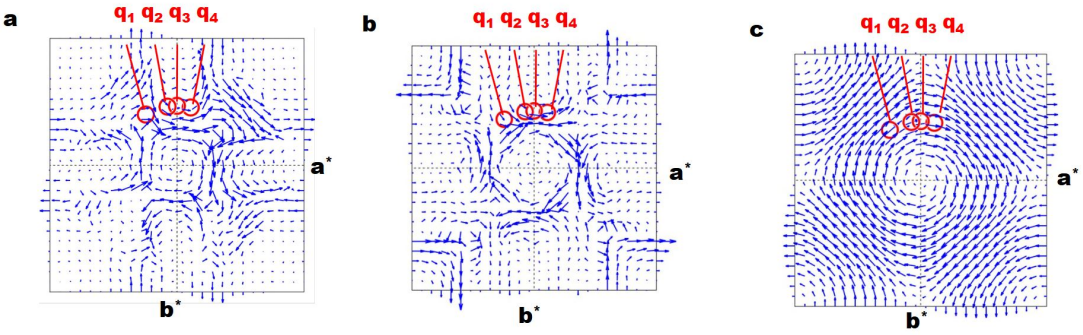

Supplementary Figure 12: Weighted chiral motion of the modes. These are a linear combination of several modes in the vicinity of the chiral modes, each weighted by their respective mode effective charges.

References

[1] Peña, M. A. & Fierro, J. L. G. Chemical structures and performance of perovskite oxides. *Chemical Reviews* **101**, 1981–2018 (2001). URL https://doi.org/10.1021/cr980129f.

[2] Leroy, L. *et al.* Antiferrodistortive and ferroeletric phase transitions in freestanding films of srtio3. *Nano Letters* **25**, 7651–7657 (2025). URL https://doi.org/10.1021/acs.nanolett.4c05664.

[3] Appleby, D. J. R. *et al.* Ferroelectric properties in thin film barium titanate grown using pulsed laser deposition. *Journal of Applied Physics* **116**, 124105 (2014). URL https://doi.org/10.1063/1.4895050.

[4] Ueda, H. *et al.* Chiral phonons in quartz probed by x-rays. *Nature* **618**, 946–950 (2023). URL https://www.nature.com/articles/s41586-023-06016-5.

[5] Ueda, H. *et al.* Chiral phonons in polar linbo3. *Nature Communications* **17**, 212 (2025). URL https://doi.org/10.1038/s41467-025-66911-5.

[6] Nag, A. *et al.* Circular dichroism in resonant inelastic x-ray scattering from birefringence in cuo. *Phys. Rev. Res.* **7**, L022047 (2025). URL https://doi.org/10.1103/PhysRevResearch.7.L022047.

[7] Zhang, L. & Niu, Q. Chiral phonons at high-symmetry points in monolayer hexagonal lattices. *Phys. Rev. Lett.* **115**, 115502 (2015). URL https://doi.org/10.1103/PhysRevLett.115.115502.

[8] Chaudhary, S., Romao, C. P. & Juraschek, D. M. Anomalous phonon magnetic moments (2025). URL https://doi.org/10.48550/arXiv:2504.19121. 2504.19121.

[9] Juraschek, D. M. & Spaldin, N. A. Orbital magnetic moments of phonons. *Phys. Rev. Mater.* **3**, 064405 (2019). URL https://doi.org/10.1103/PhysRevMaterials.3.064405.

[10] Ament, L. J., Veenendaal, M. V., Devereaux, T. P., Hill, J. P. & Brink, J. V. D. Resonant inelastic x-ray scattering studies of elementary excitations. *Rev. Mod. Phys.* **83**, 705–767 (2011). URL https://doi.org/10.1103/RevModPhys.83.705.

[11] Gonze, X. & Lee, C. Dynamical matrices, born effective charges, dielectric permittivity tensors, and interatomic force constants from density-functional perturbation theory. *Phys. Rev. B* **55**, 10355–10368 (1997). URL https://link.aps.org/doi/10.1103/PhysRevB.55.10355.